

Prewhitening of magnetotelluric data using a robust filter and robust PARCOR

Yoshiya Usui¹⁾

¹⁾ Earthquake Research Institute, The University of Tokyo

Abstract

The magnetotelluric method is one of the most effective techniques for probing subsurface structures. It utilizes frequency response functions between electromagnetic field components as input data for inversion to estimate the electrical resistivity structure of the subsurface. One of the most frequently used approaches for estimating the magnetotelluric response function is ensemble averaging, in which each observed time series is divided into segments of constant length. However, this method can result in power leakage at frequencies distant from the main lobe of the spectral window, leading to a severe bias in the estimates of the response functions. Prewhitening is a highly effective approach for reducing spectral leakage by flattening the power of the observed data prior to calculation of their Fourier transforms. However, it is known that the standard prewhitening method, which uses a least-squares approach, is not robust to outliers in the time series. Therefore, this study investigates the advantages and disadvantages of a prewhitening method that uses a robust filter and robust partial autocorrelation coefficient (PARCOR) algorithms, compared to the standard prewhitening method. By applying the robust method to synthetic and real-world MT data, it was found that the robust filter effectively removed spike noise. However, combining the robust filter and robust PARCOR resulted in excessive alteration of the data, including signals and time delays of the boxcar-like feature of time series. This combined use is therefore not recommended for magnetotelluric data processing. When the robust filter was not used, prewhitening using the robust PARCOR provided comparable magnetotelluric response functions to those obtained by the standard prewhitening method. Because the former took more than 100 times longer than the latter, the standard prewhitening method seems to be more cost effective, at least in the examples in the present work, although further investigation would be desirable to determine the usefulness of the robust PARCOR algorithm.

Keywords: prewhitening, robust statistics, magnetotelluric, time-series analysis, spectral analysis

1. Introduction

The magnetotelluric (MT) method is a passive electromagnetic (EM) exploration method used to image subsurface electrical resistivity structures based on EM field data observed on the Earth's surface. This method can be used to investigate electrical resistivity structures from the near surface to the mantle. Because of its effectiveness in probing subsurface structures, the MT method has been used for a variety of purposes worldwide, including the exploration of structures under seismogenic zones (e.g., Aizawa *et al.*, 2021; Usui *et al.*, 2021, 2024a), volcanic areas (e.g., Usui *et al.*, 2017;

Heise *et al.*, 2024), and the oceanic mantle (e.g., Tada *et al.* 2014; Baba *et al.*, 2017). In the inversion for estimating subsurface electrical resistivity structures, the frequency response functions between observed EM field components are used as input data. Therefore, it is important to be able to accurately estimate the frequency response functions to obtain reliable inversion results.

A frequently used approach for estimating MT response functions is ensemble averaging (e.g., Bendat and Piersol, 2010). In this method, observed time series are divided into segments of constant length (Fig. 1).

*e-mail: yusui@eri.u-tokyo.ac.jp (〒113-0032 東京都文京区弥生 1-1-1)

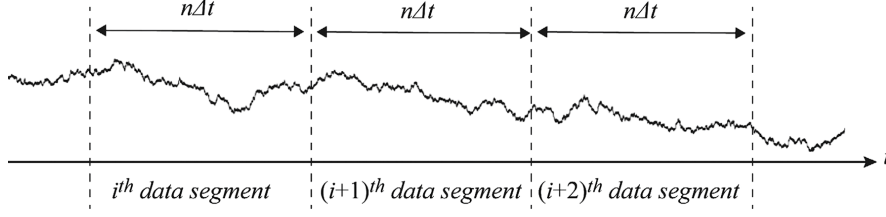


Fig. 1. Schematic of ensemble averaging method. Time-series data are divided into a number of data segments with a fixed length ($n\Delta t$ in this figure). The Fourier transform of each data segment is used as a sample to estimate the MT response function.

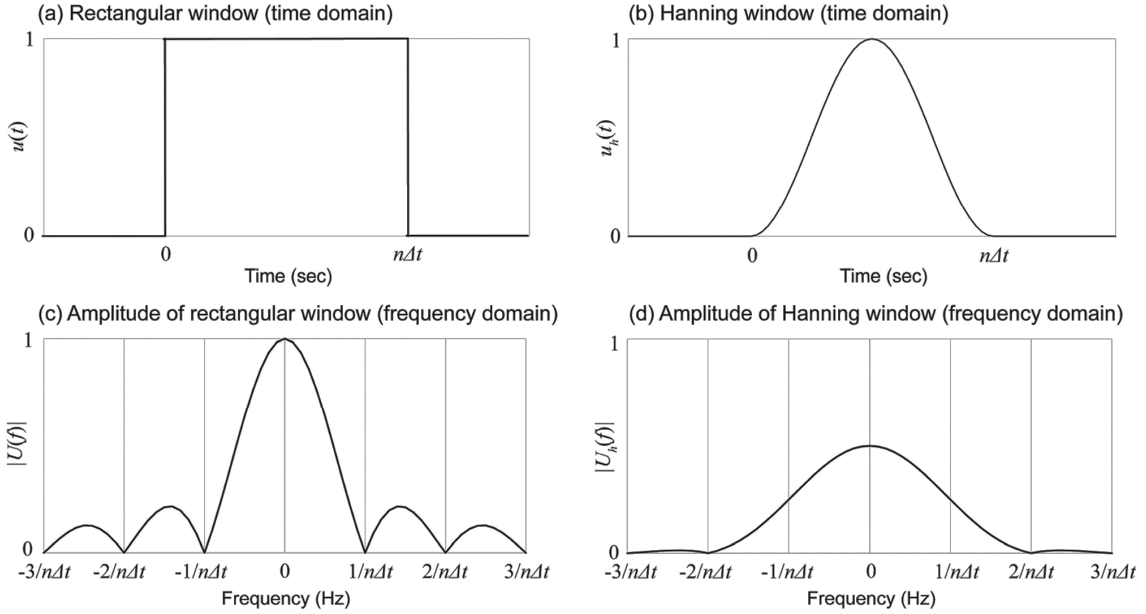


Fig. 2. (a) Rectangular time window. (b) Hanning window. (c) Amplitude of rectangular window in frequency domain. (d) Amplitude of Hanning window in frequency domain.

After calculating the Fourier transforms of each segment, the auto- and cross-spectral density functions of the EM field components are calculated by ensemble averaging, and the MT response functions are determined from the spectral density functions. The finite Fourier transform of the time series of a segment can be viewed as the Fourier transform of an infinite time series multiplied by a rectangular time window $u(t)$ (Fig. 2a) (Bendat and Piersol, 2010), where

$$u(t) = \begin{cases} 1 & 0 \leq t \leq n\Delta t, \\ 0 & \text{otherwise.} \end{cases} \quad (1)$$

In the frequency domain, the Fourier transform of the time series of a segment is the convolution of the Fourier transforms of $u(t)$ and the unlimited time series, denoted as $v(t)$, as follows.

$$\int_{-\infty}^{\infty} U(s)V(f-s)ds, \quad (2)$$

where $U(f)$ and $V(f)$ represent the Fourier transforms of $u(t)$ and $v(t)$, respectively. As shown in Fig. 2c, $|U(f)|$ has large side lobes, which allow power leakage at frequencies distant from the main lobe of the spectral window (Bendat and Piersol, 2010). These large side lobes are troublesome when analyzing MT time-series data. Since the amplitude of the EM field generally increases with decreasing frequency (e.g., Simpson and Bahr, 2005; Constable, 2015), high-power components at frequencies lower than the target frequency can significantly distort the estimates of spectral density functions in many cases. In what follows, this undesirable phenomenon is referred to as spectral

leakage.

One of the most effective methods for reducing spectral leakage is to increase the segment length ($n\Delta t$). As the segment length increases, $|U(t)|$ approaches a delta function. However, this approach decreases the number of samples used to estimate the response functions, thereby increasing the uncertainty of the estimates. Therefore, this approach is not useful unless the length of the time series is substantially longer than the period at which the response function is estimated. To remedy the spectral leakage problem, a tapered time window is commonly used (Bendat and Piersol, 2010). A popular window for such tapering is the Hanning window (Fig. 2b), which is defined as:

$$u_h(t) = \begin{cases} 1/2 \left(1 - \cos\left(\frac{2\pi t}{n\Delta t}\right) \right) & 0 \leq t \leq n\Delta t, \\ 0 & \text{otherwise.} \end{cases} \quad (3)$$

Fig. 2d shows the absolute value of the Fourier transform of $u_h(t)$, denoted as $U_h(f)$. The side lobes of $|U_h(f)|$ are notably smaller than those of $|U(f)|$, although the width of the main lobe of $|U_h(f)|$ is twice that of $|U(f)|$ (Fig. 2). However, as demonstrated in Sections 3 and 4, such tapering still cannot sufficiently suppress spectral leakage.

Another powerful technique for preventing spectral leakage is prewhitening, which was introduced by Blackman and Tukey (1958). Tukey (1967) stated, ‘*If low frequencies are 10^3 , 10^4 , or 10^5 times as active as high ones, a not-infrequent phenomenon in physical situations, even a fairly good window is too leaky for comfortable use. The cure is not to go in for fancier windows, but rather to preprocess the data toward a flatter spectrum, to analyze this “prewhitened” series, ...*’. Prewhitening flattens the power of the observed data before calculating their Fourier transforms. However, standard prewhitening methods that use an autoregression (AR) estimator are sensitive to outliers in the time-series data (Martin and Thomson, 1982; Maronna *et al.*, 2019). To address this, the method must be made sufficiently robust to flatten the spectrum properly. In the present study, prewhitening was applied using a robust filter and robust partial autocorrelation coefficient (PARCOR) algorithms, which was originally proposed by Maronna *et al.* (2019), to the MT response function estimation

and the advantages and disadvantages of this method were investigated. The next section describes the detailed algorithms for the robust prewhitening method, and in Sections 3 and 4, these algorithms are applied to synthetic and real-world MT data.

2. Method

Prewhitening time-series data can be achieved with an AR sequence that approximately fits the time-series data (Martin and Thomson, 1982; Maronna *et al.*, 2019). If $\{y_t\}_{t=-\infty}^{\infty}$ is a zero-mean stationary time series, the p -th-order AR, denoted as AR(p), satisfies the following difference equation (Hamilton, 1994):

$$y_t = \phi_1 y_{t-1} + \phi_2 y_{t-2} + \dots + \phi_p y_{t-p} + \varepsilon_t, \quad (4)$$

where $\{\varepsilon_t\}_{t=-\infty}^{\infty}$ is a white noise sequence, i.e., a collection of independent and identically distributed (iid) random noise with zero mean.

There are several algorithms to estimate the AR coefficients ϕ_1, \dots, ϕ_p (Kitagawa, 2005). One of the most well-known is the Durbin-Levinson algorithm (Brockwell and Davis, 2002). The Durbin-Levinson algorithm determines the AR coefficients that minimize the following expression:

$$E[(y_t - \phi_1 y_{t-1} - \phi_2 y_{t-2} - \dots - \phi_p y_{t-p})^2], \quad (5)$$

which represents the expectation of the mean-squared error between y_t and a linear combination of y_{t-1}, \dots, y_{t-p} . A linear combination that minimizes Eq. (5) is the minimum mean squared error (MMSE) linear predictor (Brockwell and Davis, 2002). Coefficients ϕ_1, \dots, ϕ_p are computed recursively. The coefficients at the m -th iteration, denoted by $\phi_{m,1}, \dots, \phi_{m,m}$, are computed using the following:

$$\phi_{m,m} = \{\gamma(m) - \sum_{i=1}^{m-1} \phi_{m-1,m} \gamma(m-i)\} / v_{m-1}, \quad (6)$$

$$\begin{pmatrix} \phi_{m,1} \\ \vdots \\ \phi_{m,m-1} \end{pmatrix} = \begin{pmatrix} \phi_{m-1,1} \\ \vdots \\ \phi_{m-1,m-1} \end{pmatrix} - \phi_{m,m} \begin{pmatrix} \phi_{m-1,m-1} \\ \vdots \\ \phi_{m-1,1} \end{pmatrix}, \quad (7)$$

$$\begin{aligned}
v_m &= \gamma(0) - (\phi_{m,1}, \dots, \phi_{m,m}) \begin{pmatrix} \gamma(1) \\ \vdots \\ \gamma(m) \end{pmatrix} \\
&= v_{m-1}(1 - \phi_{m,m}^2),
\end{aligned} \tag{8}$$

$$\gamma(j) = \text{Cov}(y_t, y_{t+j}) = \text{Cov}(y_t, y_{t-j}), \tag{9}$$

where $\phi_{1,1} = \gamma(1)/\gamma(0)$, $v_0 = \gamma(0)$ and $\gamma(j)$ ($j = 0, \dots, m$), which represents the autocovariance function of $\{y_t\}_{t=-\infty}^{\infty}$. The coefficients at the m -th iteration $\phi_{m,1}, \dots, \phi_{m,m}$ are equivalent to the coefficients ϕ_1, \dots, ϕ_m that minimize Eq. (5).

Maronna *et al.* (2019) showed that $\phi_{m,m}$ for the Durbin-Levinson algorithm, which is called the partial autocorrelation of $\{y_t\}_{t=-\infty}^{\infty}$ (Brockwell and Davis, 2002), corresponds to the regression coefficient between the memory- $(m-1)$ forward and backward MMSE prediction residuals. The memory- $(m-1)$ forward MMSE predictor $\hat{y}_{t,m-1}$ and residual $\hat{u}_{t,m-1}$ are defined as follows:

$$\hat{y}_{t,m-1} = \sum_{i=1}^{m-1} \phi_{m-1,i} y_{t-i}, \tag{10}$$

$$\hat{u}_{t,m-1} = y_t - \hat{y}_{t,m-1}. \tag{11}$$

The memory- $(m-1)$ backward MMSE predictor $\hat{y}_{t-m,m-1}^*$ and residual $\hat{u}_{t-m,m-1}^*$ are given by:

$$\hat{y}_{t-m,m-1}^* = \sum_{i=1}^{m-1} \phi_{m-1,i} y_{t-m+i}, \tag{12}$$

$$\hat{u}_{t-m,m-1}^* = y_{t-m} - \hat{y}_{t-m,m-1}^*. \tag{13}$$

Then, the MMSE linear predictor of $\hat{u}_{t,m-1}$ with respect to $\hat{u}_{t-m,m-1}^*$,

$$\zeta_m^* = \arg \min_{\zeta_m} E[(\hat{u}_{t,m-1} - \zeta_m \hat{u}_{t-m,m-1}^*)^2], \tag{14}$$

is equivalent to the partial autocorrelation (Maronna *et al.*, 2019). If one calculates ζ_m by the least-squares method from the memory- $(m-1)$ forward and backward MMSE residuals, this algorithm corresponds to the PARCOR method described by Kitagawa (2005). The optimal order of the AR model can be determined by the Akaike information criterion (AIC):

$$\text{AIC}(m) = n[\log(2\pi v_m) + 1] + 2(m+1), \tag{15}$$

as shown in Kitagawa (2005). In Eq. (15), n is the sample number in time-series data. The first term on

the right-hand side is composed of the maximum log-likelihood, whereas the second term depends on the AR order (m) (Kitagawa, 2005).

Because outliers in time-series data can lead to bias and inflated variability in the AR coefficients obtained by the least-squares method, the robust prewhitening method that uses a robust filter and robust PARCOR algorithms has been introduced (Maronna *et al.*, 2019). As the first step in making the method robust, $y_{t-m}, y_{t-m+1}, \dots, y_{t-1}$ in the memory- $(m-1)$ forward and backward MMSE prediction residuals (Eqs. (11) and (13)) are replaced by a modified time series obtained through a robust filter to avoid the propagation of the influence of outlying data (Martin and Thomson, 1982; Maronna *et al.*, 2019). The calculation algorithm for the robust filtered values is based on an approximate conditional mean robust filter (Masreliez, 1975; Martin, 1979). Details of the robust filter algorithm are provided in Appendix A.

In the second step, a robust PARCOR method was used to calculate the partial autocorrelation. In this study, Eq. (14) is replaced with a univariate regression S-estimator (Rousseeuw and Yohai, 1984), which seeks a coefficient ζ_m^* that minimizes the robust scale estimate, $\hat{\sigma}_m$, of the regression residuals. Specifically, if the number of time-series data is n , Eq. (14) is replaced by

$$\zeta_m^* = \arg \min_{\zeta_m} \hat{\sigma}_m(\hat{\mathbf{u}}(\zeta_m)), \tag{16}$$

where $\hat{\mathbf{u}}(\zeta_m) \in \mathbb{R}^{n-m}$ is the residual vector

$$\hat{\mathbf{u}}(\zeta_m) = \begin{pmatrix} \hat{u}_{m+1,m-1} - \zeta_m \hat{u}_{1,m-1}^* \\ \vdots \\ \hat{u}_{n,m-1} - \zeta_m \hat{u}_{n-m,m-1}^* \end{pmatrix}. \tag{17}$$

The fast algorithm for the S-estimator proposed by Salibian-Barrera and Yohai (2006) was used for robust estimation. These authors used random subsampling to select multiple initial estimates. However, in this study, 11 samples evenly distributed over $[-1, 1]$ were used as the initial estimates because ζ_m has a limited range. The I-step of the fast algorithm (Salibian-Barrera and Yohai, 2006) was applied to each candidate until convergence was achieved.

The robust filter and PARCOR were alternately applied. First, the partial autocorrelation ζ_1^* was deter-

mined using the S-estimator:

$$\zeta_1^* = \arg \min_{\zeta_1} \hat{\sigma}_1(\hat{\mathbf{u}}(\zeta_1)), \quad (18)$$

$$\hat{\mathbf{u}}(\zeta_1) = \begin{pmatrix} y_2 - \zeta_1 y_1 \\ \vdots \\ y_n - \zeta_1 y_{n-1} \end{pmatrix}. \quad (19)$$

The robust filter was then applied to time-series data with ζ_1^* and the minimum, $\hat{\sigma}_1$. Subsequently, the partial autocorrelation ζ_2^* was determined using Eq. (16). The other AR coefficients were calculated by replacing $\phi_{m,m}$ in Eq. (7) with ζ_2^* . The robust filter was applied to the time-series data again with AR coefficients and the minimum, $\hat{\sigma}_2$. These operations were repeated until m reached the maximum value. The optimal order of the AR model can be selected using the robust AIC for the S-estimator (Tharmaratnam and Claeskens, 2013):

$$AIC.S(m) = 2(n-m)\ln(\hat{\sigma}_m) + 2\frac{K_{s,m}}{J_{s,m}}, \quad (20)$$

$$J_{s,m} = \frac{1}{n-m} \sum_{i=1}^{n-m} \rho'_d \left(\frac{\hat{u}_{m+i,m-1} - \zeta_m \hat{u}_{i,m-1}^*}{\hat{\sigma}_m} \right) \left(\frac{\hat{u}_{i,m-1}^*}{\hat{\sigma}_m} \right)^2, \quad (21)$$

$$K_{s,m} = \frac{1}{n-m} \sum_{i=1}^{n-m} \rho''_d \left(\frac{\hat{u}_{m+i,m-1} - \zeta_m \hat{u}_{i,m-1}^*}{\hat{\sigma}_m} \right) \left(\frac{\hat{u}_{i,m-1}^*}{\hat{\sigma}_m} \right)^2. \quad (22)$$

Here, ρ'_d and ρ''_d are the first- and second-order derivatives of the loss function of the bisquare weight (Maronna *et al.*, 2019), respectively. Using the AR coefficients that minimize $AIC.S$, denoted as $\hat{\phi}_1 \cdots \hat{\phi}_{\hat{p}}$, the AR residuals can be calculated using

$$y_t - \hat{\phi}_1 y_{t-1} - \cdots - \hat{\phi}_{\hat{p}} y_{t-\hat{p}}. \quad (23)$$

The Fourier transforms of the AR residuals were computed using a fast Fourier transform (FFT) after tapering with Hanning window (Bendat and Piersol, 2010). Subsequently, the influence of the AR filter was adjusted by dividing the Fourier transform by

$$1 - \sum_{k=1}^{\hat{p}} \hat{\phi}_k \exp\left(-\frac{j2\pi f k}{f_s}\right), \quad (24)$$

where j is an imaginary unit, f is the frequency, and f_s is the sampling frequency. Corrected Fourier transforms

were used for the response function estimation after instrument calibration. Although Martin and Thomson (1982) and Maronna *et al.* (2019) directly used filtered time-series data to compute Fourier transforms, in the present study, the original time-series data were used for the subsequent response function estimation, and filtered time-series data were used only to estimate the AR coefficients. This approach avoids the risk that incorrectly altered signals are directly used in response function estimation.

3. Application to synthetic MT data

The robust prewhitening method was applied to a synthetic time-series dataset to investigate its advantages and disadvantages. The synthetic data were similar to those used by Usui *et al.* (2024b) and were obtained from the response functions computed using the Oblique Conductor model of Tietze *et al.* (2015). The sampling frequency was 24 Hz, and the data length was 72 h (three days). Gaussian and spike noise were added to all channels of the local and remote stations. The Gaussian and spike noise for each channel and station were mutually independent. Because the power of cultural noise usually varies with time, the amplitude of the Gaussian noise was modulated sinusoidally over 24 h. Specifically, the Gaussian noise was multiplied by an amplification factor, as shown in Fig. 3a. Spike noise occurred with a probability of one in ten thousand in the synthetic time series. Fig. 3b–e shows the resulting synthetic time series for the E_x and B_x channels. Fig. 4 compares the power spectra for the EM field components before and after the addition of noise. The power of the noise was larger than that of the signal in periods of less than approximately 30 s in the magnetic field data, whereas the noise in the electric field data influenced a wider period range, with its power being larger than that of the signal in periods of less than approximately 100 s.

To analyze the data, the overlapped processing technique (Bendat and Piersol, 2010) was used, and each time series was divided into segments with 50% overlap. The maximum segment length was 524288, which was halved iteratively down to 128, resulting in 13 segment lengths. For each segment length, response functions were estimated at the third and fourth fre-

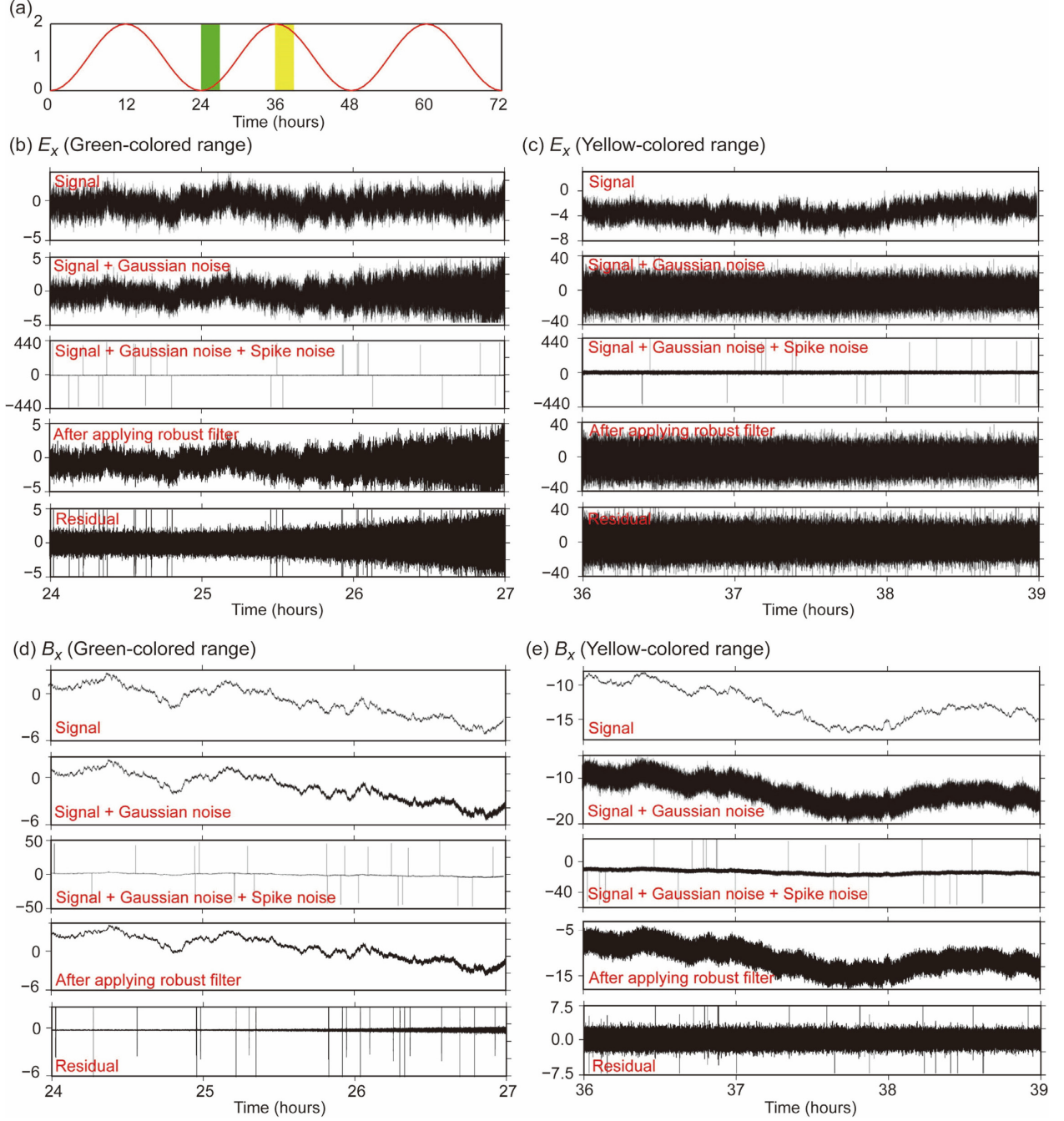


Fig. 3. (a) Multiplication factor for raw Gaussian noise. The green portion corresponds to the time range of (b) and (d), and the yellow portion corresponds to the time range of (c) and (e). (b, c) Synthetic time series for the x-component of the local electric field (mV/km). (d, e) Synthetic time series for the x-component of the local magnetic field (nT). In (b), (c), (d), and (e), the panels from top to bottom show the time series for the signal, signal + Gaussian noise, signal + Gaussian noise + spike noise, time series after applying the robust filter ($\hat{x}_{t|t}$ in Eq. (A41)), and residuals of AR model (ϵ_t in Eq. (4)).

quencies, that is, $3/n\Delta t$ and $4/n\Delta t$ Hz. The maximum order of the AR models used for prewhitening was 100. To estimate the response functions, a robust remote reference method was employed, applying the Huber weight (Huber, 1964) followed by a more severe weight function proposed by Chave and Thomson (1989, 2004).

The impedance tensors were obtained using four different prewhitening methods: no prewhitening, standard (non-robust) prewhitening, prewhitening with only robust PARCOR, and prewhitening with both robust PARCOR and filtering. In the standard prewhitening method, the PARCOR method was used with a least-squares

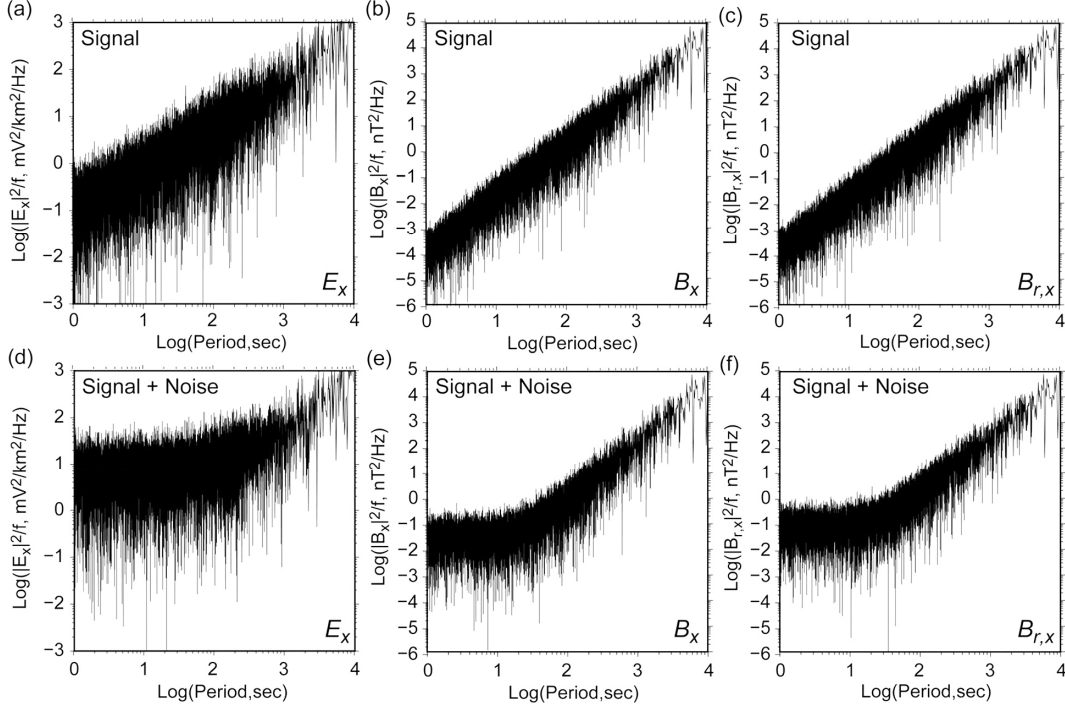


Fig. 4. Power spectra of x-components of synthetic EM field at local MT (left and middle panels) and reference stations (right panel). (a–c) Power spectra of EM field containing signals only. (d–f) Power spectra of EM field containing signals and noise.

approach. Mean values were subtracted from the respective channels before applying prewhitening.

Fig. 5a, b shows the histories of the AIC and AIC.S for the E_x - and B_x -components. The AIC was computed for standard prewhitening, while AIC.S was computed for the two robust prewhitening methods. For both components, the AIC and AIC.S decreased with increasing AR order, except at $m=3$ for the robust prewhitening methods. Table 1 lists the AR orders that minimized the AIC and AIC.S under the constraint that $m \leq 100$. For many components, the selected AR order was 100, suggesting that the AIC and AIC.S could further decrease for $m > 100$. Fig. 5c, d depicts the histories of $\sqrt{\nu_m}$ for standard prewhitening and $\hat{\sigma}_m$ for robust prewhitening. The square root of ν_m was used because $\sqrt{\nu_m}$ and $\hat{\sigma}_m$ have the same dimension. The histories of the AIC and AIC.S have similar shapes to those of $\sqrt{\nu_m}$ and $\hat{\sigma}_m$. The sample number (n) for the time series for each channel was 6220800. Since the sample number was significantly larger than the maximum AR order ($m=100$), the maximum log-likelihood term was dominant in the AIC. The change rates for the AIC and AIC.S per single increase

in AR order were smaller than 0.01% at $m=100$.

At $m=3$, the AIC.S for the E_x -component was noticeably smaller than at higher orders. The robust scale estimate of the regression residual is used in the equations of the AIC.S (Eqs. (20), (21), and (22)), and the robust scale was locally small at $m=3$ (Fig. 5c). Because the average of the data-adaptive weights for $m=3$ was smaller than those for the other orders, the data might be excessively downweighted at $m=3$, leading to locally small AIC.S. Time series of residuals of the AR model (ε_t of Eq. (4)) are depicted at the bottoms of Fig. 3b–e. Long-period changes in the original time series disappeared in the residual time series. The robust filter altered the time series during prewhitening. The bottoms of Fig. 3b–e depict the time series after applying the robust filter ($\hat{x}_{t|t}$ in Eq. (A41)). The spike noise disappeared after the application of the robust filter, as the filter removed such noise as outliers.

Fig. 6 compares the estimated apparent resistivity and phase with the true sounding curves. Only off-diagonal components are shown to facilitate visualization. When no prewhitening was applied (Fig. 6a), the apparent resistivity was underestimated and exhibited

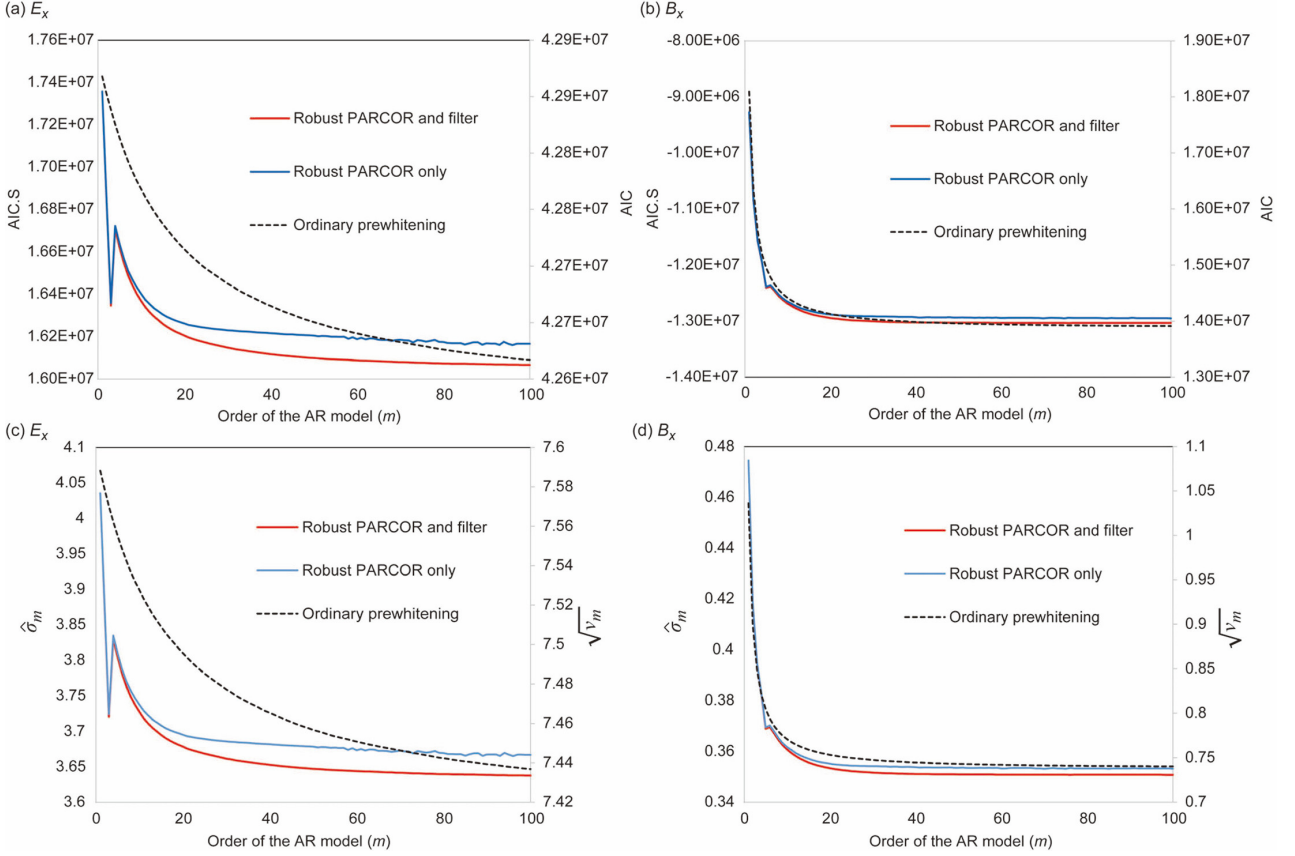


Fig. 5. Changes in AIC and $\sqrt{v_m}$ for standard prewhitening and AIC.S and $\hat{\sigma}_m$ for robust prewhitening as AR model order increases. (a, b) Changes in AIC and AIC.S for E_x - and B_x -components of synthetic data, respectively. (c, d) Changes in $\sqrt{v_m}$ and $\hat{\sigma}_m$ for E_x - and B_x -components of synthetic data, respectively. The square root of v_m is used because $\sqrt{v_m}$ and $\hat{\sigma}_m$ have the same dimension.

Table 1. AR orders selected in prewhitening for synthetic time-series data. Because the upper limit of the AR order was fixed, there is no order higher than 100.

	E_x	E_y	B_x	B_y	$B_{r,x}$	$B_{r,y}$
Ordinary prewhitening	100	100	100	100	100	100
Robust PARCOR only	96	100	100	95	91	93
Robust PARCOR and filter	100	100	76	99	99	100

oscillations. These downward biases and oscillations exceeded the error bars. To investigate the cause of this further, the response function and normalized power for the E_y - and B_x -components were computed as the ratio of the average Fourier transform of the noise-contaminated data to that of the time series containing only the signals. The common logarithms of the normalized powers are equivalent to the log (power) differences between the noise-contaminated data and signals. In the computation, the second and fifth frequencies were used in addition to the third and fourth

frequencies. The segment length was reduced by multiplying by 1/4 instead of 1/2 to avoid duplication of frequencies (e.g., the fourth frequency for 524288 length is equal to the second frequency for 262144 length). Fig. 7 shows the resultant apparent resistivity and normalized power for two different combinations of segment length (one starts from 524288 and the other starts from 262144). The increase in the normalized power of E_y with decreasing period is due to the increase in the noise-to-signal ratio in the electric field. On the other hand, the normalized power of B_x was

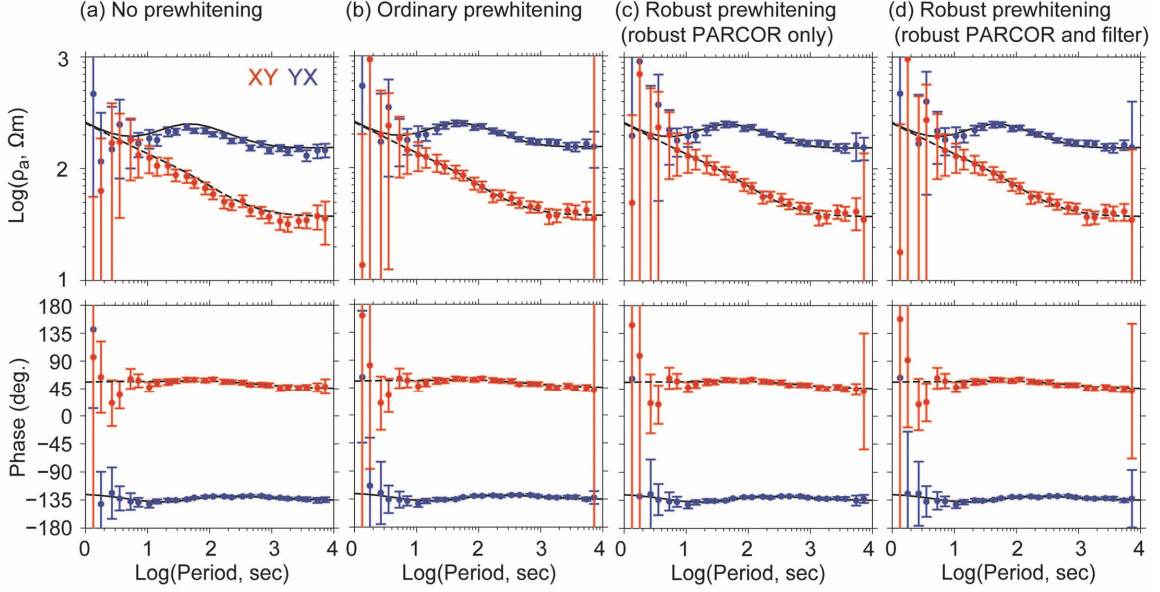


Fig. 6. Comparison of sounding curves for apparent resistivity and phase for synthetic time-series data against true sounding curves. Circles with error bars are the estimated response functions, and the solid and dashed lines indicate the true sounding curves for the yx - and xy -components, respectively. Error bars indicate the 95% confidence intervals under the assumption that the standard errors of the apparent resistivity and phase follow a Gaussian distribution.

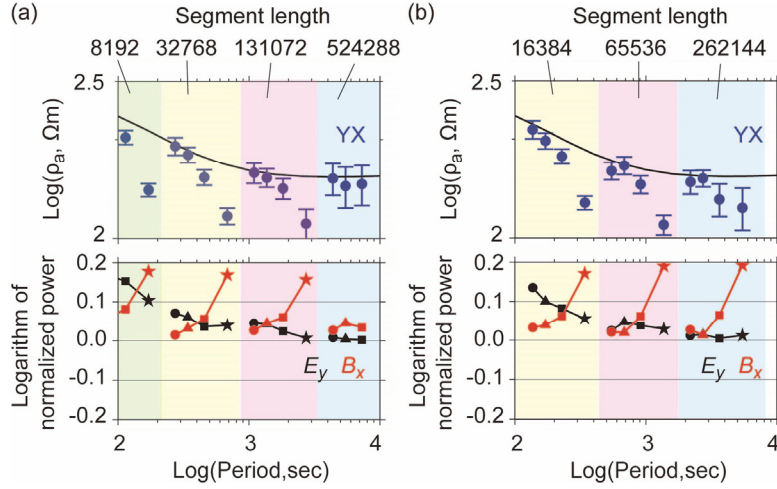


Fig. 7. Apparent resistivity of yx -component and common logarithms of normalized power of E_y - and B_x -components for synthetic time-series data. Results of the non-prewhitening case are depicted. Normalized power is defined as the ratio of the average Fourier transform of noise-contaminated data to that of the time series containing only a signal. The stars, squares, triangles, and circles in the bottom figures correspond to the normalized power at the second, third, fourth, and fifth frequencies, respectively, for each segment length. The segment length was reduced by multiplying by $1/4$ to avoid the duplication of frequencies. The segment length of (a) starts from 524288, whereas the segment length of (b) starts from 262144.

greater than zero in all periods, indicating that the powers of the B_x component were overestimated, even when the noise power was relatively low. Because the Fourier transforms were directly calculated from the raw data in the non-prewhitening case, the power leakage at longer periods significantly distorted the

Fourier transforms, resulting in an overestimation of the B_x power. In addition, an undulation of the normalized power of B_x was observed. Fig. 7 illustrates that, even if the segment length is the same, the lower the frequency, the larger the overestimation of the B_x component. It appears that the undulation of the normal-

ized power of B_x was caused by the differences in the distortions and that the Fourier transforms at lower frequency could be distorted more severely. This was probably because the power of the B_x -component increases with decreasing frequency on the logarithmic scale. As a result, the longer the period, the larger the underestimation of the apparent resistivity.

When prewhitening was applied, the downward bias and undulation of the apparent resistivity were

not noticeable (Fig. 6b–d). Fig. 8b–d shows that the power spectra for the B_x component after prewhitening are flat. All prewhitening methods provided comparable response functions in this example. However, when a lower AR order was used, specifically 20, for the prewhitening, noticeable differences appeared. Fig. 9 shows an enlarged view of the apparent resistivity of the y_x -component and the normalized power of the E_y - and B_x -components for this case. The downward

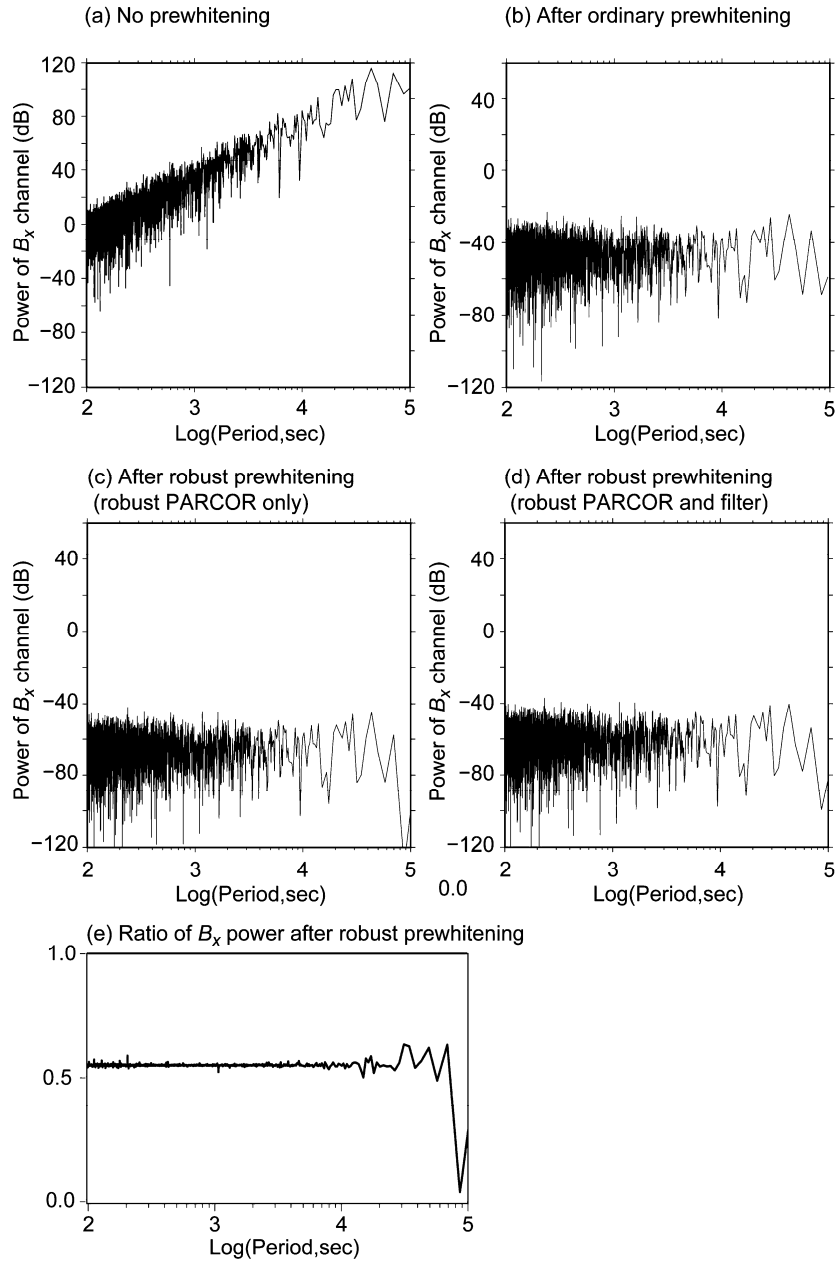


Fig. 8. (a–d) Comparison of power spectra of B_x -component before and after prewhitening. Decibels are used as the units for the vertical axes because Fourier transforms do not have physical units after AR filtering in the prewhitening method. To clarify differences between (c) and (d), the ratio of the power shown in (c) to that shown in (d) is depicted in (e).

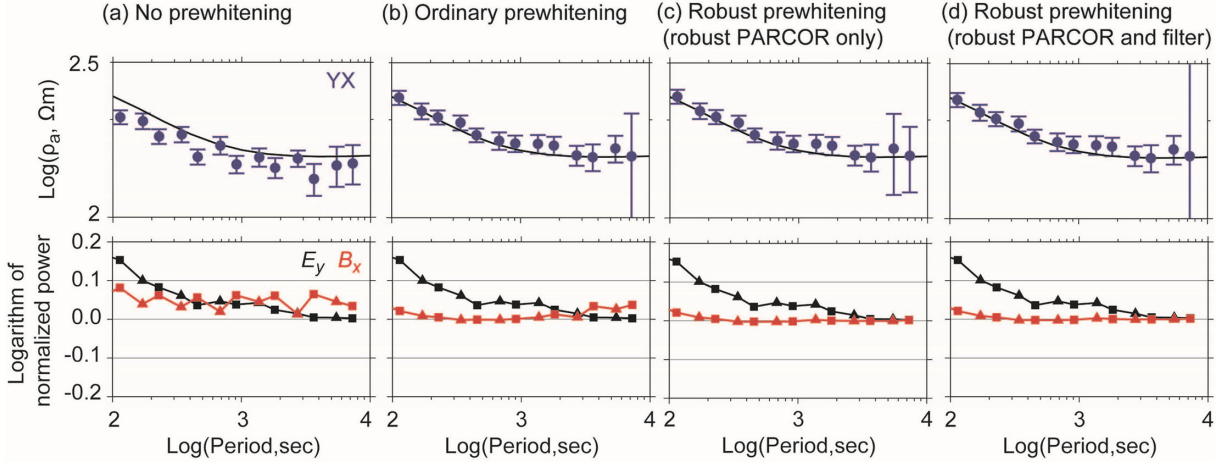


Fig. 9. Apparent resistivity and normalized power for AR order of 20. The top panels are enlarged views of the apparent resistivity, while the bottom panels show the common logarithms of the normalized powers of the E_y - and B_x -components. Normalized power is defined as the ratio of the average Fourier transform of noise-contaminated data to that of the time series data containing only a signal. The Fourier transforms after prewhitening are used in the lower panels of (b), (c), and (d). The squares and triangles in the bottom figures correspond to the normalized power at the third and fourth frequencies, respectively, for each segment length.

bias of the apparent resistivity and overestimation of the B_x component appeared at the longest four periods when the standard prewhitening method was used (Fig. 9b), whereas such undesirable features were not noticeable when robust prewhitening was used (Fig. 9c, d). It would appear that, at least in this example, the standard prewhitening method needs a higher AR order to sufficiently flatten the power of the data compared to robust prewhitening.

There was a significant difference in computation times among the three prewhitening methods. The computation times required for standard prewhitening and robust prewhitening using only the robust PARCOR were 114 s and 19451 s, respectively. Because the S-estimator seeks a solution that minimizes the scale starting from a number of initial values (11 initial values in this study) and performs iterative calculations for each initial value, it requires a significantly longer time than standard prewhitening. The computation time for robust prewhitening using both robust PARCOR and filtering was 55246 s. If the robust filter was used, the computation time increased by more than two times compared to when only robust PARCOR was used. As all prewhitening methods yielded comparable response functions, the standard prewhitening method seems to be cost effective in this example.

4. Application to real-world data

Next, prewhitening methods were applied to real-world data measured at the Kakioka Magnetic Observatory, Japan (Kakioka Magnetic Observatory, 2013a, b). The 10-Hz sampling data for the electric field (Kakioka Magnetic Observatory, 2013a) and magnetic field (Kakioka Magnetic Observatory, 2013b) were employed. For the remote reference method, data from Memambetsu (Kakioka Magnetic Observatory, 2013c) were used. To maximize the influence of noise, I used EM time-series data in a time period in which the activity of the geomagnetic field was weak, specifically, five days from November 14 to 18, 2020. For time periods in which the geomagnetic field activity was not low, significantly smoother MT response functions could be obtained (e.g., Fujii *et al.*, 2015). The response functions were estimated at the second and third frequencies for each segment length. Except for these differences, the calculation conditions were the same as those in the previous synthetic data analysis.

Fig. 10a, b shows the histories of the AIC and AIC.S for the E_x - and B_x -components, and Table 2 lists the AR orders that minimized the AIC and AIC.S under the constraint that $m \leq 100$. The shapes of the AIC and AIC.S histories are similar to those of $\sqrt{\nu_m}$ and $\hat{\sigma}_m$, respectively (Fig. 10c, d), as in the case of the synthetic data analysis. As for the E_x -component, the

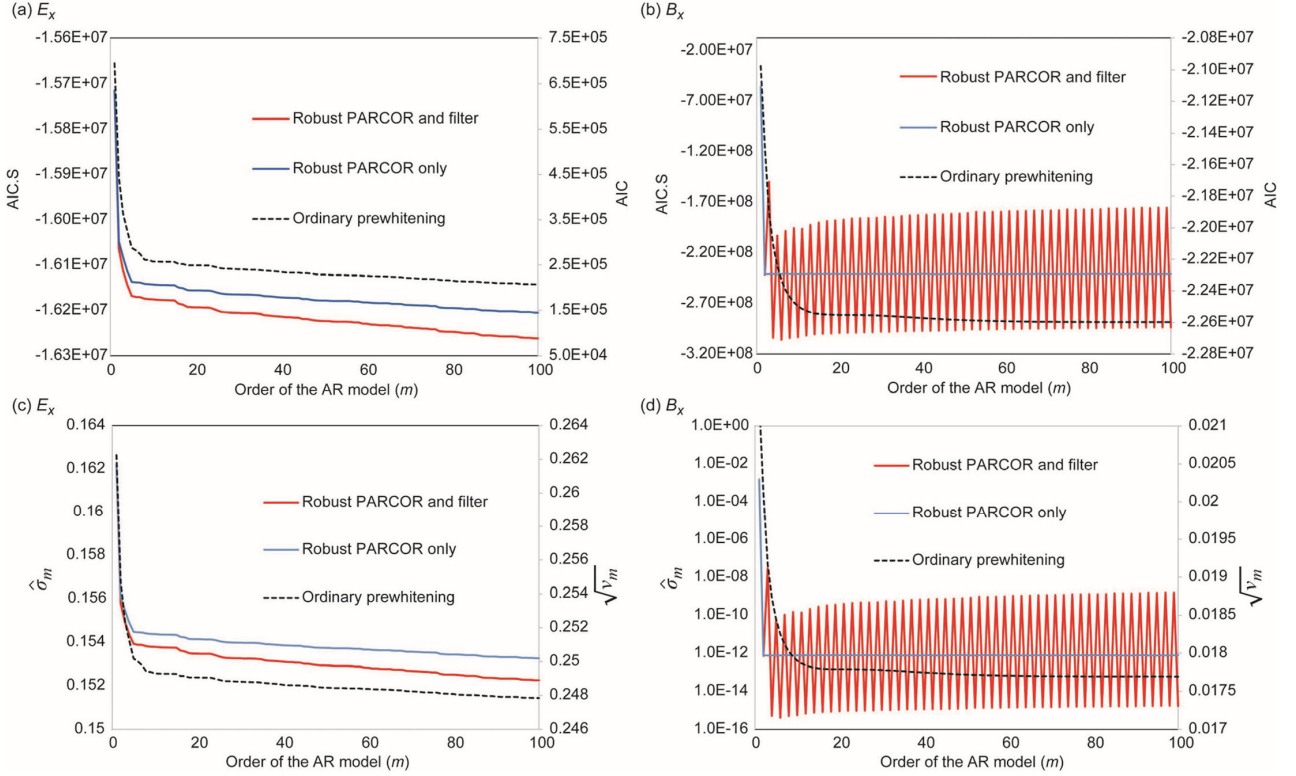


Fig. 10. Changes in AIC and $\sqrt{v_m}$ for standard prewhitening and AIC.S and $\hat{\sigma}_m$ for robust prewhitening as AR model order increases. (a, b) Changes in AIC and AIC.S for E_x - and B_x -components at Kakioka Magnetic Observatory, respectively. (c, d) Changes in $\sqrt{v_m}$ and $\hat{\sigma}_m$ for E_x - and B_x -components at Kakioka Magnetic Observatory, respectively. It should be noted that only the left vertical axis of (d) uses a logarithmic scale. The square root of v_m is used because $\sqrt{v_m}$ and $\hat{\sigma}_m$ have the same dimension.

Table 2. AR orders selected in prewhitening for time-series data at Kakioka (E_x , E_y , B_x , and B_y) and Memambetsu ($B_{r,x}$ and $B_{r,y}$). Because the upper limit of the AR order was fixed, there is no order higher than 100.

	E_x	E_y	B_x	B_y	$B_{r,x}$	$B_{r,y}$
Ordinary prewhitening	100	100	100	100	100	100
Robust PARCOR only	100	100	14	10	100	85
Robust PARCOR and filter	100	100	6	4	100	9

AIC and AIC.S nearly monotonically decreased with increasing AR order, even at $m=100$. On the other hand, the histories of the AIC and AIC.S for the B_x -component heavily depended on the prewhitening method. The AIC for the standard prewhitening method monotonically decreased with increasing AR order, as in the case of the E_x -component. The AIC.S for the robust prewhitening methods sharply decreased at a few AR orders, and the changes at higher orders were relatively small. It was possible that the robust PARCOR downweighted the variations requiring higher AR orders as outliers in determining the autocorrelation.

When both robust PARCOR and filtering were applied to the B_x component data, the AIC.S oscillated with increasing AR order (Fig. 10b). As described below, the robust filter presumably removed most of the signals, as well as noise. This excessive alteration of data might have caused the oscillations.

The raw time series, the time series altered by the robust filter, and the residuals for the AR model for the E_x - and B_x -components are compared in Fig. 11. The boxcar-like feature in the raw time series of the E_x -component, which is downwardly convex, is delayed by a few seconds in the time series altered by

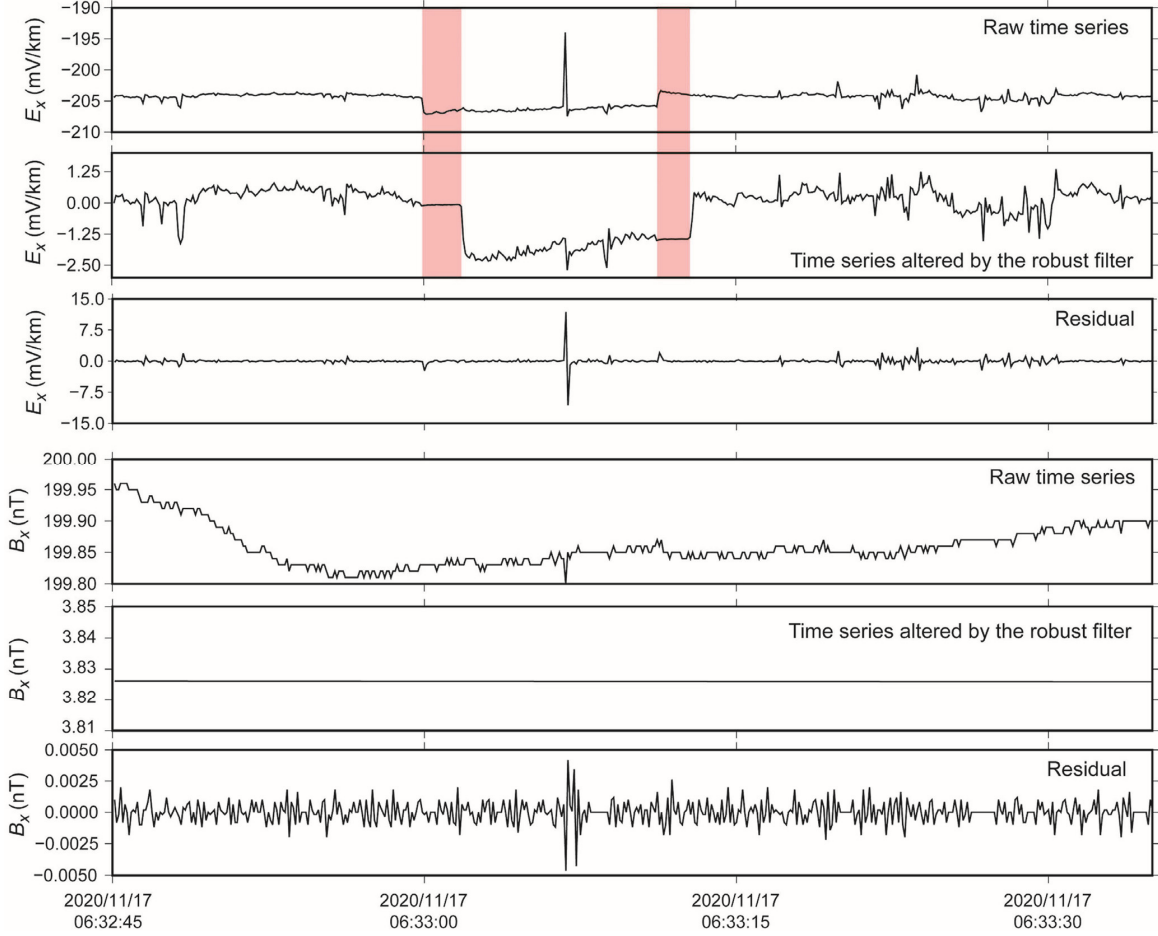


Fig. 11. Comparison of raw time series, time series altered by robust filter ($\hat{x}_{t|t}$ in Eq. (A41)), and residuals for AR model (ε_t in Eq. (4)) of the E_x - and B_x -components at Kakioka Magnetic Observatory, Japan.

the robust filter. The reason for this delay is as follows. In the red-colored time ranges in Fig. 11, the raw time series were altered based on Eq. (A41) in Appendix A because the difference between the raw and conditional mean values was larger than the thresholds in Eq. (A37). On the other hand, on the right sides of the red-colored ranges, raw data or only slightly altered values were used because the difference between the raw and conditional mean values was relatively small. Such a delay can be avoided by changing the adjustable parameters of the robust filter, i.e., thresholds a and b in Eqs. (A37) and (A40) and the maximum number of consecutive alterations (k) (see the last sentence of Appendix A). Actually, when $k=10$ was used, the time shift of the boxcar-like feature did not occur. However, the appropriate setting of these parameters probably depends on the data, and it seems impossible to determine prior to data analysis. The residuals of the

B_x -components are nearly flat (Fig. 11), implying that most of the signals, as well as noise, were removed as outliers by the robust filter.

Fig. 12 shows the resultant sounding curves for the apparent resistivity and phase. When no prewhitening was applied, the resultant sounding curves were discontinuous, and zigzag features were noticeable in the apparent resistivity (Fig. 12a), as in the synthetic data example. When prewhitening was applied, the response functions significantly improved (Fig. 12b–d). However, at periods of 100–1000 s, the apparent resistivity of the xx - and yx -components obtained using the robust PARCOR and filtering (Fig. 12h) is noticeably different from those obtained with standard prewhitening or robust prewhitening with only robust PARCOR (Fig. 12f, g). When the robust filter was used, the change in the power of the B_x -component after prewhitening is sharp from 100 to 1000 s (Fig. 13h), suggesting that the

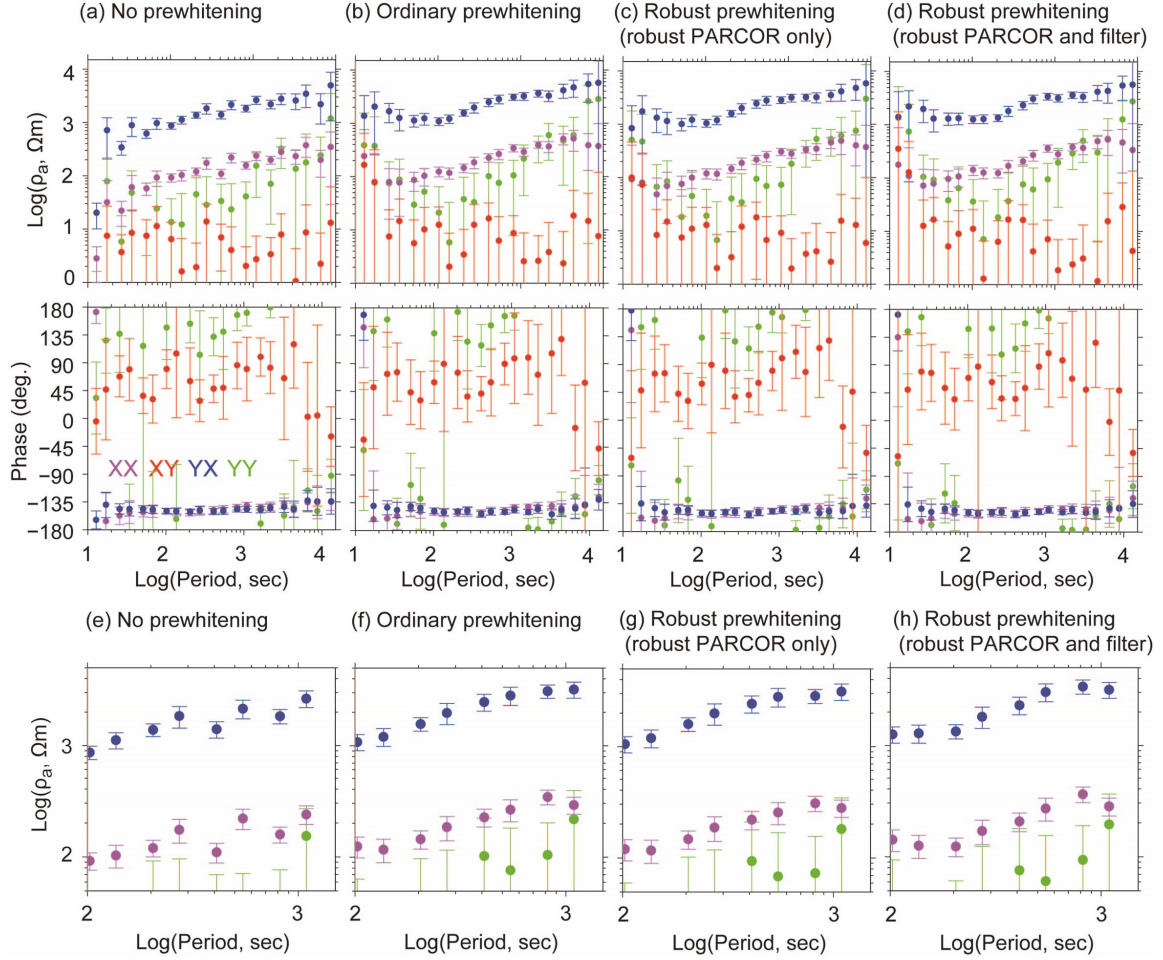


Fig. 12. (a–d) Estimated sounding curves for apparent resistivity and phase with error bars at Kakioka Magnetic Observatory, Japan. Error bars indicate the 95% confidence intervals under the assumption that the standard errors of the apparent resistivity and phase follow a Gaussian distribution. (e–h) Enlarged views of apparent resistivity for each case.

prewhitening using the robust PARCOR and filtering failed to estimate AR coefficients adequately.

This study identified negative effects associated with the combined use of the robust filter and robust PARCOR: the excessive alteration of data and time delays in boxcar-like time series features. These issues likely hindered proper estimation of the AR coefficients. Although such undesirable results may be avoided by changing the adjustable parameters of the robust filter, it seems impossible to know the appropriate values of those parameters in advance. Therefore, careful parameter selection through trial and error is necessary. Based on these findings, it can be concluded that the combined use of the robust filter and robust PARCOR is not recommended for MT data processing.

As in the synthetic data example, the computation time significantly increased with robust prewhitening

compared to standard prewhitening. In concrete terms, the computation time for standard prewhitening and robust prewhitening with only the robust PARCOR were 80 and 12218 s, respectively, and that for robust prewhitening with both the robust PARCOR and filtering was 235113 s. Since standard prewhitening gave comparable response functions to those obtained by robust prewhitening with only robust PARCOR in a significantly shorter time, the standard prewhitening method is also considered to be cost effective in this example. However, the sensitiveness of the standard prewhitening method to outliers has been recognized (Martin and Thomson, 1982; Maronna *et al.*, 2019), and Chave and Thomson (1989, 2004) mentioned the importance of the robust prewhitening in MT data processing, although they used a different robust prewhitening algorithm. Thus, further investigation is warranted

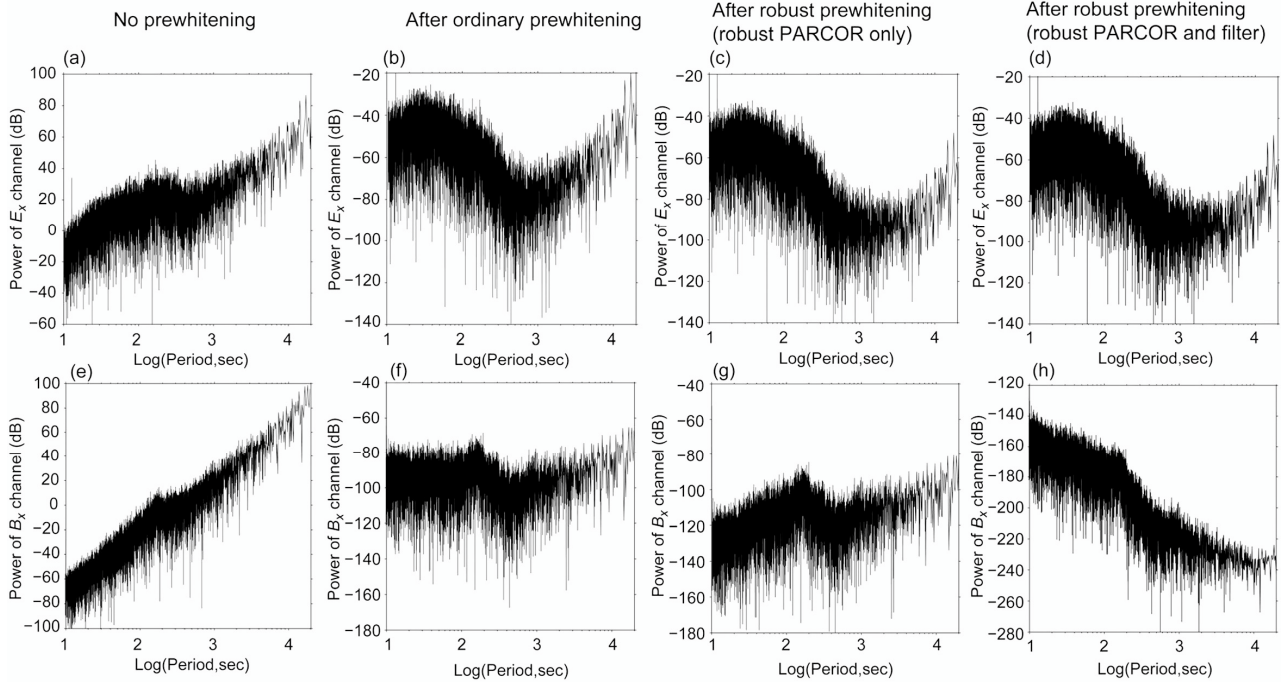


Fig. 13. (a–d) Comparison of power spectra of E_x -component before and after prewhitening. (e–h) Comparison of power spectra for the B_x -component before and after pre-whitening. Decibels are used as the units for the vertical axes because Fourier transforms do not have physical units after AR filtering in the prewhitening method.

to determine the usefulness of the robust PARCOR algorithm.

5. Conclusion

When the MT response function is estimated using ensemble averaging, spectral leakage can lead to a severe bias in the resultant estimates. Prewhitening is one of the most powerful tools for preventing spectral leakage. However, it is known that the standard prewhitening method using a least-squares approach is not robust to outliers in the time series. To address this issue, a robust prewhitening method was applied using a robust filter and robust PARCOR algorithms to synthetic and real-world MT data and its advantages and disadvantages were investigated. The main findings are as follows.

- The importance of using prewhitening was confirmed for processing time-series data from MT measurements. If prewhitening was not used, the apparent resistivity exhibited significant underestimation and undulation.
- The robust filter could remove spike noise. However, negative effects were found to be associated with the combined use of the robust filter and robust

PARCOR: the excessive alteration of data and time delay of the boxcar-like feature of time series. Thus, it was concluded that their combined use is not recommended for MT data processing.

- In the examples in the present work, prewhitening using the robust PARCOR provided comparable MT response functions to those obtained by standard prewhitening if the robust filter was not used. Because the former took more than 100 times longer than the latter, the standard prewhitening method seems to be cost effective.

As previous studies have pointed out the sensitiveness of standard prewhitening to outliers in time series data and the importance of robust prewhitening in MT data processing, further investigation would be desirable to determine the usefulness of the robust PARCOR algorithm.

Acknowledgments

This study was supported by the Yamaguchi Educational and Scholarship Foundation. I would like to thank Tsutomu Ogawa (the University of Tokyo) for his comments, which helped me to improve the manuscript. Several figures were created using Generic Mapping

Tools (Wessel *et al.*, 2013).

References

- Aizawa, K., S. Takakura, H. Asaue, K. Koike, R. Yoshimura, K. Yamazaki, et al., 2021, Electrical conductive fluid-rich zones and their influence on the earthquake initiation, growth, and arrest processes: observations from the 2016 Kumamoto earthquake sequence, Kyushu Island, Japan. *Earth Planets Space*, **73**, 1–12.
- Baba, K., J. Chen, M. Sommer, H. Utada, W. H. Geissler, W. Jokat, et al., 2017, Marine magnetotellurics imaged no distinct plume beneath the Tristan da Cunha hotspot in the southern Atlantic Ocean. *Tectonophysics*, **716**, 52–63.
- Bendat, J.S. and A.G. Piersol, 2010, *Random Data: Analysis and Measurement Procedures*, 4th ed., John Wiley & Sons, Hoboken, 604 pp.
- Blackman, R.B. and J.W. Tukey, 1958, *The Measurement of Power Spectra*, Dover Publ. Inc., New York, 190 pp.
- Brockwell, P.J. and R.A. Davis, 2002, *Introduction to time series and forecasting*, 2nd ed., Springer, New York, 434 pp.
- Chave, A.D. and D.J. Thomson, 1989, Some comments on magnetotelluric response function estimation. *J. Geophys. Res.*, **94**, 14215–14225.
- Chave, A.D. and D.J. Thomson, 2004, Bounded influence magnetotelluric response function estimation. *Geophys. J. Int.*, **157**, 988–1006.
- Constable, S., 2015, Geomagnetic Induction Studies, in “*Treatise on Geophysics*”, 2nd ed., Vol 5. edited by G. Schubert, Oxford: Elsevier., pp. 219–254.
- Fujii, I., T. Ookawa, S. Nagamachi and T. Owada, 2015, The characteristics of geoelectric fields at Kakioka, Kanoya, and Memambetsu inferred from voltage measurements during 2000 to 2011. *Earth Planets Space*, **67**, 1–17.
- Hamilton, J. D., 1994, *Time series analysis*, Princeton university press, Princeton, New Jersey, 799 pp.
- Heise, W., S. Bannister, C.A. Williams, P. McGavin, T.G. Caldwell, E.A. Bertrand, et al., 2024, Magmatic priming of a phreatic eruption sequence: the 2012 Te Maari eruptions at Mt Tongariro (New Zealand) imaged by Magnetotellurics and seismicity. *Geophys. J. Int.*, **236**, 1848–1862.
- Huber, P., 1964, Robust estimation of a location parameter. *Ann. Math. Stat.*, **35**, 73–101.
- Kakioka Magnetic Observatory, 2013a, Kakioka geoelectric field 1-decisecond digital data in IAGA-2002 format [dataset], Kakioka Magnetic Observatory Digital Data Service, doi:10.48682/129bd.ed000.
- Kakioka Magnetic Observatory, 2013b, Kakioka geomagnetic field 1-decisecond digital data in IAGA-2002 format [dataset], Kakioka Magnetic Observatory Digital Data Service, doi:10.48682/186bd.ed000.
- Kakioka Magnetic Observatory, 2013c, Memambetsu geomagnetic field 1-decisecond digital data in IAGA-2002 format [dataset], Kakioka Magnetic Observatory Digital Data Service, doi:10.48682/186d7.ed000.
- Kitagawa, G., 2005, *Introduction to time series analysis*, Iwanami Shoten, Tokyo, 265 pp (in Japanese).
- Maronna, R.A., R.D. Martin, V.J. Yohai and M. Salibián-Barrera, 2019, *Robust Statistics: Theory and Methods (with R)*, 2nd ed., John Wiley & Sons, New York, 430 pp.
- Martin, R.D., 1979, Approximate conditional-mean type smoothers and interpolators, in “*Smoothing techniques for curve estimation*”, edited by Th. Gasser and M. Rosenblatt, Springer, pp. 117–143.
- Martin, R.D. and D.J. Thomson, 1982, Robust-resistant spectrum estimation. *Proceedings of the IEEE*, **70**, 1097–1115.
- Masreliez, C., 1975, Approximate non-Gaussian filtering with linear state and observation relations. *IEEE Trans. Automat. Contr.*, **20**, 107–110.
- Rousseeuw, P.J. and V. Yohai, 1984, Robust Regression by Means of S-Estimators, in “*Robust and Nonlinear Time Series Analysis*”, edited by J. Franke, W. Hardle and D. Martin, Springer-Verlag, pp. 256–272.
- Salibián-Barrera, M. and V. Yohai, 2006, A fast algorithm for S-regression estimates. *J. Comput. Graph. Statist.*, **15**, 414–427.
- Simpson, F. and K. Bahr, 2005, *Practical magnetotellurics*, Cambridge University Press, Cambridge, 254 pp.
- Tada, N., K. Baba and H. Utada, 2014, Three-dimensional inversion of seafloor magnetotelluric data collected in the Philippine Sea and the western margin of the northwest Pacific Ocean. *Geochem. Geophys. Geosyst.*, **15**, 2895–2917.
- Tharmaratnam, K. and G. Claeskens, 2013, A comparison of robust versions of the AIC based on M-, S- and MM-estimators. *Statistics*, **47**, 216–235.
- Tietze K., O. Ritter and G.D. Egbert, 2015, 3-D joint inversion of the magnetotelluric phase tensor and vertical magnetic transfer functions. *Geophys. J. Int.*, **203**, 1128–1148.
- Tukey, J.W., 1967, An introduction to the calculations of numerical spectrum analysis, in “*Proceedings of the Advanced Seminar on Spectral Analysis of Time Series*”, edited by B. Harris, John Wiley & Sons.
- Usui, Y., Y. Ogawa, K. Aizawa, W. Kanda, T. Hashimoto, T. Koyama, et al., 2017, Three-dimensional resistivity structure of Asama Volcano revealed by data-space magnetotelluric inversion using unstructured tetrahedral elements. *Geophys. J. Int.*, **208**, 1359–1372.
- Usui, Y., M. Uyeshima, T. Ogawa, R. Yoshimura, N. Oshiman, S. Yamaguchi, et al., 2021, Electrical resistivity structure around the Atotsugawa fault, central Japan, revealed by a new 2-D inversion method combining wideband-MT and Network-MT data sets. *J. Geophys. Res.: Solid Earth*, **126**, e2020JB020904.
- Usui, Y., M. Uyeshima, H. Hase, H. Ichihara, K. Aizawa, T. Koyama, et al., 2024a, Three-dimensional electrical resistivity structure beneath a strain concentration area in the back-arc side of the northeastern Japan arc. *J. Geophys. Res.: Solid Earth*, **129**, e2023JB028522.
- Usui, Y., M. Uyeshima, S. Sakanaka, T. Hashimoto, M. Ichiki, T. Kaida, et al., 2024b, New robust remote reference estimator using robust multivariate linear regression. *Geophys. J. Int.*, **238**, 943–959.
- Wessel, P., W.H.F. Smith, R. Scharroo, J. Luis and F. Wobbe, 2013, Generic mapping tools: improved version released. *EOS, Trans. Am. Geophys. Un.*, **94**, 409–410.

Appendix A: Robust filter algorithm

Martin (1979) applied the filtering method originally proposed by Masreliez (1975) to the AR model. In the

present study, the approximate conditional mean robust filter of Martin (1979) was used to avoid propagating the influence of outliers. This appendix shows the details of the algorithm. In the subsequent description, it is assumed that $\{y_t\}_{t=-\infty}^{\infty}$ is a zero-mean stationary time series. Using the state vector $\mathbf{x}_t \in \mathbb{R}^p$, Martin (1979) expressed the p -th order AR model by

$$\mathbf{x}_t = \Phi \mathbf{x}_{t-1} + \varepsilon_t, \quad (\text{A1})$$

$$y_t = \mathbf{h}^T \mathbf{x}_t + v_t, \quad (\text{A2})$$

$$\mathbf{x}_t = (x_t, x_{t-1}, \dots, x_{t-p+1})^T, \quad (\text{A3})$$

$$\Phi = \begin{pmatrix} \phi_1 & \dots & \phi_{p-1} & \phi_p \\ \mathbf{I}_{(p-1) \times (p-1)} & & & \mathbf{0}_{p-1} \end{pmatrix}, \quad (\text{A4})$$

$$\varepsilon_t = (\varepsilon_t, 0, \dots, 0)^T, \quad (\text{A5})$$

$$\mathbf{h} = (1, 0, \dots, 0)^T, \quad (\text{A6})$$

where $\phi_1, \phi_2, \dots, \phi_p$ indicate the coefficients of the p -th-order AR model; $\mathbf{I}_{(p-1) \times (p-1)}$ is the $(p-1) \times (p-1)$ identity matrix; and $\mathbf{0}_{p-1}$ is the zero vector in \mathbb{R}^{p-1} . It is assumed that the sequences $\{\varepsilon_t\}_{t=-\infty}^{\infty}$ and $\{v_t\}_{t=-\infty}^{\infty}$ are mutually independent noises with zero means and that the elements of each sequence are individually independent and identically distributed (iid). It is also assumed that \mathbf{x}_t is independent of ε_i ($i > t$) and v_t . Because \mathbf{x}_t follows the p -th order AR relationship and y_t is the observed value, v_t indicates the deviation from the p -th order AR model, including the influence of outliers in time-series data.

In the approximate conditional mean robust filter, the conditional expectation of the state vector

$$\hat{\mathbf{x}}_{t|t} = \int_{\mathbb{R}^p} \mathbf{x}_t f_{\mathbf{x}_t|Y_1, \dots, Y_t}(\mathbf{x}_t|y_1, \dots, y_t) d\mathbf{x}_t, \quad (\text{A7})$$

is selected as a robust filter value. In Eq. (A7), \mathbf{X}_t and Y_1, \dots, Y_t indicate the random variables for the state vector and observed values, respectively, and $f_{\mathbf{x}_t|Y_1, \dots, Y_t}$ is the conditional probability density function (PDF) for the state vector. Masreliez (1975) proposed a recursion algorithm to calculate conditional expectation. For the derivation of the recursion algorithm, it is necessary to introduce a conditional mean vector and conditional covariances:

$$\begin{aligned} & \tilde{\mathbf{x}}_{t|t-1} \\ &= \int_{\mathbb{R}^p} \mathbf{x}_t f_{\mathbf{x}_t|Y_1, \dots, Y_{t-1}}(\mathbf{x}_t|y_1, \dots, y_{t-1}) d\mathbf{x}_t, \end{aligned} \quad (\text{A8})$$

$$\begin{aligned} \mathbf{P}_t &= \int_{\mathbb{R}^p} (\hat{\mathbf{x}}_{t|t} - \mathbf{x}_t)(\hat{\mathbf{x}}_{t|t} - \mathbf{x}_t)^T \\ & \quad f_{\mathbf{x}_t|Y_1, \dots, Y_t}(\mathbf{x}_t|y_1, \dots, y_t) d\mathbf{x}_t, \end{aligned} \quad (\text{A9})$$

$$\begin{aligned} \mathbf{M}_t &= \int_{\mathbb{R}^p} (\tilde{\mathbf{x}}_{t|t-1} - \mathbf{x}_t)(\tilde{\mathbf{x}}_{t|t-1} - \mathbf{x}_t)^T \\ & \quad f_{\mathbf{x}_t|Y_1, \dots, Y_{t-1}}(\mathbf{x}_t|y_1, \dots, y_{t-1}) d\mathbf{x}_t. \end{aligned} \quad (\text{A10})$$

The conditional mean $\tilde{\mathbf{x}}_{t|t-1}$ is an estimate of \mathbf{x}_t given y_1, \dots, y_{t-1} , and \mathbf{P}_t and \mathbf{M}_t are the conditional covariances given y_1, \dots, y_t and given y_1, \dots, y_{t-1} , respectively. From Eq. (A1), the following relationship can be obtained:

$$\tilde{\mathbf{x}}_{t|t-1} = \Phi \hat{\mathbf{x}}_{t-1|t-1}. \quad (\text{A11})$$

With the aid of Bayes' theorem,

$$\begin{aligned} & f_{\mathbf{x}_t|Y_1, \dots, Y_t}(\mathbf{x}_t|y_1, \dots, y_t) \\ &= \frac{f_{Y_1, \dots, Y_t|\mathbf{x}_t}(y_1, \dots, y_t|\mathbf{x}_t) f_{\mathbf{x}_t}(\mathbf{x}_t)}{f_{Y_1, \dots, Y_t}(y_1, \dots, y_t)}, \end{aligned} \quad (\text{A12})$$

$$\begin{aligned} & f_{\mathbf{x}_t|Y_1, \dots, Y_{t-1}}(\mathbf{x}_t|y_1, \dots, y_{t-1}) \\ &= \frac{f_{Y_1, \dots, Y_{t-1}|\mathbf{x}_t}(y_1, \dots, y_{t-1}|\mathbf{x}_t) f_{\mathbf{x}_t}(\mathbf{x}_t)}{f_{Y_1, \dots, Y_{t-1}}(y_1, \dots, y_{t-1})}, \end{aligned} \quad (\text{A13})$$

the following relationship can be obtained:

$$\begin{aligned} & \frac{f_{\mathbf{x}_t|Y_1, \dots, Y_t}(\mathbf{x}_t|y_1, \dots, y_t)}{f_{\mathbf{x}_t|Y_1, \dots, Y_{t-1}}(\mathbf{x}_t|y_1, \dots, y_{t-1})} \\ &= \frac{f_{Y_t|Y_1, \dots, Y_{t-1}, \mathbf{x}_t}(y_t|y_1, \dots, y_{t-1}, \mathbf{x}_t)}{f_{Y_t|Y_1, \dots, Y_{t-1}}(y_t|y_1, \dots, y_{t-1})} \\ &= \frac{f_{Y_t|\mathbf{x}_t}(y_t|\mathbf{x}_t)}{f_{Y_t|Y_1, \dots, Y_{t-1}}(y_t|y_1, \dots, y_{t-1})}, \end{aligned} \quad (\text{A14})$$

where the second equality holds because the random variable y_t is determined only from \mathbf{x}_t and v_t . Therefore, using Eq. (A14), Eq. (A7) can be transformed into

$$\begin{aligned} & \hat{\mathbf{x}}_{t|t} \\ &= \mathbf{M}_t \frac{\int_{\mathbb{R}^p} f_{Y_t|\mathbf{x}_t}(y_t|\mathbf{x}_t) \mathbf{M}_t^{-1}(\mathbf{x}_t - \tilde{\mathbf{x}}_{t|t-1}) f_{\mathbf{x}_t|Y_1, \dots, Y_{t-1}}(\mathbf{x}_t|y_1, \dots, y_{t-1}) d\mathbf{x}_t}{f_{Y_t|Y_1, \dots, Y_{t-1}}(y_t|y_1, \dots, y_{t-1})} \\ & \quad + \tilde{\mathbf{x}}_{t|t-1}. \end{aligned} \quad (\text{A15})$$

Because \mathbf{x}_t is independent of v_t , $f_{Y_t|\mathbf{x}_t}(y_t|\mathbf{x}_t)$ can be expressed as

$$\begin{aligned} f_{Y_t|\mathbf{x}_t}(y_t|\mathbf{x}_t) &= f_{Y_t|\mathbf{x}_t}(\mathbf{h}^T \mathbf{x}_t + v_t|\mathbf{x}_t) \\ &= f_{V_t}(y_t - \mathbf{h}^T \mathbf{x}_t), \end{aligned} \quad (\text{A16})$$

where V_t is a random variable for v_t . Using Eq. (A16), Eq. (A15) can be transformed into

$$\begin{aligned} \hat{\mathbf{x}}_{t|t} &= \mathbf{M}_t \\ &\frac{\int_{\mathbb{R}^p} f_{V_t}(y_t - \mathbf{h}^T \mathbf{x}_t) \mathbf{M}_t^{-1}(\mathbf{x}_t - \tilde{\mathbf{x}}_{t|t-1}) f_{\mathbf{x}_t|Y_1, \dots, Y_{t-1}}(\mathbf{x}_t|y_1, \dots, y_{t-1}) d\mathbf{x}_t}{f_{Y_t|Y_1, \dots, Y_{t-1}}(y_t|y_1, \dots, y_{t-1})} \\ &+ \tilde{\mathbf{x}}_{t|t-1}. \end{aligned} \quad (\text{A17})$$

An additional assumption of the recursion algorithm is that the conditional PDF $f_{\mathbf{x}_t|Y_1, \dots, Y_{t-1}}$ is Gaussian (Masreliez, 1975), that is,

$$\begin{aligned} f_{\mathbf{x}_t|Y_1, \dots, Y_{t-1}}(\mathbf{x}_t|y_1, \dots, y_{t-1}) \\ &= \frac{1}{\sqrt{(2\pi)^p \det(\mathbf{M}_t)}} \exp \\ &\left(-\frac{1}{2}(\mathbf{x}_t - \tilde{\mathbf{x}}_{t|t-1})^T \mathbf{M}_t^{-1}(\mathbf{x}_t - \tilde{\mathbf{x}}_{t|t-1}) \right), \end{aligned} \quad (\text{A18})$$

$$\begin{aligned} &\frac{\partial f_{\mathbf{x}_t|Y_1, \dots, Y_{t-1}}(\mathbf{x}_t|y_1, \dots, y_{t-1})}{\partial \mathbf{x}_t} \\ &= -\mathbf{M}_t^{-1}(\mathbf{x}_t - \tilde{\mathbf{x}}_{t|t-1}) \end{aligned} \quad (\text{A19})$$

$$f_{\mathbf{x}_t|Y_1, \dots, Y_{t-1}}(\mathbf{x}_t|y_1, \dots, y_{t-1}).$$

Using Eq. (A19), Eq. (A17) can be transformed into

$$\begin{aligned} \hat{\mathbf{x}}_{t|t} &= \tilde{\mathbf{x}}_{t|t-1} - \frac{\mathbf{M}_t}{f_{Y_t|Y_1, \dots, Y_{t-1}}(y_t|y_1, \dots, y_{t-1})} \\ &\int_{\mathbb{R}^p} f_{V_t}(y_t - \mathbf{h}^T \mathbf{x}_t) \\ &\frac{\partial f_{\mathbf{x}_t|Y_1, \dots, Y_{t-1}}(\mathbf{x}_t|y_1, \dots, y_{t-1})}{\partial \mathbf{x}_t} d\mathbf{x}_t. \end{aligned} \quad (\text{A20})$$

By applying partial integration and using Eq. (A16), integration of the right-hand side of Eq. (A20) can be transformed into

$$\begin{aligned} &\int_{\mathbb{R}^p} f_{V_t}(y_t - \mathbf{h}^T \mathbf{x}_t) \frac{\partial f_{\mathbf{x}_t|Y_1, \dots, Y_{t-1}}(\mathbf{x}_t|y_1, \dots, y_{t-1})}{\partial \mathbf{x}_t} d\mathbf{x}_t \\ &= \int_{\mathbb{R}^p} \mathbf{h} f'_{V_t}(y_t - \mathbf{h}^T \mathbf{x}_t) \\ & f_{\mathbf{x}_t|Y_1, \dots, Y_{t-1}}(\mathbf{x}_t|y_1, \dots, y_{t-1}) d\mathbf{x}_t \\ &= \mathbf{h} f'_{Y_t|Y_1, \dots, Y_{t-1}}(y_t|y_1, \dots, y_{t-1}). \end{aligned} \quad (\text{A21})$$

Using Eqs. (A20) and (A21), the following equation can be obtained to update the conditional expectation for the state vector:

$$\hat{\mathbf{x}}_{t|t} = \tilde{\mathbf{x}}_{t|t-1} - \frac{f'_{Y_t|Y_1, \dots, Y_{t-1}}(y_t|y_1, \dots, y_{t-1})}{f_{Y_t|Y_1, \dots, Y_{t-1}}(y_t|y_1, \dots, y_{t-1})} \mathbf{M}_t \mathbf{h}. \quad (\text{A22})$$

Next, equations are derived to update the conditional covariance matrices. A new conditional covariance matrix is introduced:

$$\begin{aligned} &\int_{\mathbb{R}^p} (\tilde{\mathbf{x}}_{t|t-1} - \mathbf{x}_t)(\tilde{\mathbf{x}}_{t|t-1} - \mathbf{x}_t)^T \\ & f_{\mathbf{x}_t|Y_1, \dots, Y_t}(\mathbf{x}_t|y_1, \dots, y_t) d\mathbf{x}_t \\ &= -\frac{\mathbf{M}_t}{f_{Y_t|Y_1, \dots, Y_{t-1}}(y_t|y_1, \dots, y_{t-1})} \\ &\int_{\mathbb{R}^p} \frac{\partial f_{\mathbf{x}_t|Y_1, \dots, Y_{t-1}}(\mathbf{x}_t|y_1, \dots, y_{t-1})}{\partial \mathbf{x}_t} \\ & (\mathbf{x}_t - \tilde{\mathbf{x}}_{t|t-1})^T f_{V_t}(y_t - \mathbf{h}^T \mathbf{x}_t) d\mathbf{x}_t \end{aligned} \quad (\text{A23})$$

where Eqs. (A14), (A16), and (A19) are used. Notably, the conditional covariance matrix in Eq. (A23) differs from \mathbf{P}_t because $\tilde{\mathbf{x}}_{t|t-1}$ is used instead of $\hat{\mathbf{x}}_{t|t}$. By applying partial integration, the integration of Eq. (A23) can be transformed into

$$\begin{aligned} &-\mathbf{I}_p \int_{\mathbb{R}^p} f_{\mathbf{x}_t|Y_1, \dots, Y_{t-1}}(\mathbf{x}_t|y_1, \dots, y_{t-1}) f_{V_t}(y_t - \mathbf{h}^T \mathbf{x}_t) d\mathbf{x}_t \\ &- \int_{\mathbb{R}^p} f_{\mathbf{x}_t|Y_1, \dots, Y_{t-1}}(\mathbf{x}_t|y_1, \dots, y_{t-1}) \\ &\frac{\partial f_{V_t}(y_t - \mathbf{h}^T \mathbf{x}_t)}{\partial \mathbf{x}_t} (\mathbf{x}_t - \tilde{\mathbf{x}}_{t|t-1})^T d\mathbf{x}_t \end{aligned} \quad (\text{A24})$$

where $\mathbf{I}_p \in \mathbb{R}^{p \times p}$ is the $p \times p$ identity matrix. The first term in Eq. (A24) can be transformed into

$$-\mathbf{I}_p f_{Y_t|Y_1, \dots, Y_{t-1}}(y_t|y_1, \dots, y_{t-1}), \quad (\text{A25})$$

and using Eq. (A19), the second term can be transformed into

$$\begin{aligned}
 & \int_{\mathbb{R}^p} \frac{\partial f_{V_t}(y_t - \mathbf{h}^T \mathbf{x}_t)}{\partial \mathbf{x}_t} \left(\frac{\partial f_{\mathbf{X}_t|Y_1, \dots, Y_{t-1}}(\mathbf{x}_t|y_1, \dots, y_{t-1})}{\partial \mathbf{x}_t} \right)^T d\mathbf{x}_t \mathbf{M}_t \\
 &= -\mathbf{h} \int_{\mathbb{R}^p} f''_{V_t}(y_t - \mathbf{h}^T \mathbf{x}_t) f_{\mathbf{X}_t|Y_1, \dots, Y_{t-1}}(\mathbf{x}_t|y_1, \dots, y_{t-1}) d\mathbf{x}_t \mathbf{h}^T \mathbf{M}_t \quad (\text{A26}) \\
 &= -\mathbf{h} f''_{Y_t|Y_1, \dots, Y_{t-1}}(y_t|y_1, \dots, y_{t-1}) \mathbf{h}^T \mathbf{M}_t,
 \end{aligned}$$

where partial integration is applied again. Using Eqs. (A24), (A25), and (A26), Eq. (A23) can be transformed into

$$\begin{aligned}
 & \int_{\mathbb{R}^p} (\tilde{\mathbf{x}}_{t|t-1} - \mathbf{x}_t)(\tilde{\mathbf{x}}_{t|t-1} - \mathbf{x}_t)^T \\
 & f_{\mathbf{X}_t|Y_1, \dots, Y_t}(\mathbf{x}_t|y_1, \dots, y_t) d\mathbf{x}_t \quad (\text{A27}) \\
 &= \mathbf{M}_t + \frac{f''_{Y_t|Y_1, \dots, Y_{t-1}}(y_t|y_1, \dots, y_{t-1})}{f_{Y_t|Y_1, \dots, Y_{t-1}}(y_t|y_1, \dots, y_{t-1})} \mathbf{M}_t \mathbf{h} \mathbf{h}^T \mathbf{M}_t.
 \end{aligned}$$

With the aid of Eq. (A27), an equation for updating the conditional covariance \mathbf{P}_t can be obtained:

$$\begin{aligned}
 \mathbf{P}_t &= \mathbf{M}_t + \frac{f''_{Y_t|Y_1, \dots, Y_{t-1}}(y_t|y_1, \dots, y_{t-1})}{f_{Y_t|Y_1, \dots, Y_{t-1}}(y_t|y_1, \dots, y_{t-1})} \mathbf{M}_t \mathbf{h} \mathbf{h}^T \mathbf{M}_t \\
 &\quad - (\tilde{\mathbf{x}}_{t|t-1} - \hat{\mathbf{x}}_{t|t})(\tilde{\mathbf{x}}_{t|t-1} - \hat{\mathbf{x}}_{t|t})^T. \quad (\text{A28})
 \end{aligned}$$

Because \mathbf{x}_t is independent of ε_{t+1} , an equation for updating the conditional covariance \mathbf{M}_{t+1} can be obtained from \mathbf{P}_t :

$$\begin{aligned}
 \mathbf{M}_{t+1} &= \int_{\mathbb{R}^p} (\Phi \hat{\mathbf{x}}_{t|t} - \Phi \mathbf{x}_t - \varepsilon_{t+1}) \\
 & (\Phi \hat{\mathbf{x}}_{t|t} - \Phi \mathbf{x}_t - \varepsilon_{t+1})^T \quad (\text{A29}) \\
 & f_{\mathbf{X}_t|Y_1, \dots, Y_t}(\mathbf{x}_t|y_1, \dots, y_t) d\mathbf{x}_t
 \end{aligned}$$

$$= \Phi \mathbf{P}_t \Phi^T + \mathbf{Q},$$

$$\mathbf{Q} = \begin{pmatrix} \sigma_\varepsilon^2 & 0 & \dots & 0 \\ 0 & 0 & \dots & 0 \\ \vdots & \vdots & \ddots & \vdots \\ 0 & 0 & \dots & 0 \end{pmatrix}, \quad (\text{A30})$$

where σ_ε^2 is the variance of $\{\varepsilon_t\}_{t=-\infty}^\infty$. Hence, the state vector $\hat{\mathbf{x}}_{t|t}$ can be calculated by recursions using Eqs. (A11), (A22), (A28), and (A29).

The conditional PDF $f_{Y_t|Y_1, \dots, Y_{t-1}}$ is the convolution of f_{V_t} with the conditional PDF for the first component of \mathbf{x}_t (Martin, 1979). Because PDF $f_{\mathbf{X}_t|Y_1, \dots, Y_{t-1}}$ follows a multivariate Gaussian distribution, the conditional PDF for the first component of \mathbf{x}_t can be expressed as

$$\begin{aligned}
 & f_{X_t|Y_1, \dots, Y_{t-1}}(x_t|y_1, \dots, y_{t-1}) \\
 &= \frac{1}{\sqrt{2\pi m_t}} \exp\left(-\frac{1}{2} \left(\frac{x_t - \tilde{x}_{t|t-1}}{m_t}\right)^2\right), \quad (\text{A31})
 \end{aligned}$$

where m_t is the (1, 1) element of the covariance matrix \mathbf{M}_t , and $\tilde{x}_{t|t-1}$ is the first component of $\tilde{\mathbf{x}}_{t|t-1}$. For example, if the random variable V_t is assumed to follow a zero-mean Gaussian distribution

$$f_{V_t}(v_t) = \frac{1}{\sqrt{2\pi\sigma_v^2}} \exp\left(-\frac{1}{2} \left(\frac{v_t}{\sigma_v}\right)^2\right), \quad (\text{A32})$$

the conditional PDF $f_{Y_t|Y_1, \dots, Y_{t-1}}$ is given by

$$\begin{aligned}
 & f_{Y_t|Y_1, \dots, Y_{t-1}}(y_t|y_1, \dots, y_{t-1}) \\
 &= \frac{1}{\sqrt{2\pi(m_t + \sigma_v^2)}} \exp\left(-\frac{1}{2} \left(\frac{y_t - \tilde{x}_{t|t-1}}{m_t + \sigma_v^2}\right)^2\right). \quad (\text{A33})
 \end{aligned}$$

If Eq. (A33) is used as the conditional PDF, Eqs. (A22) and (A28) can be transformed into

$$\hat{\mathbf{x}}_{t|t} = \tilde{\mathbf{x}}_{t|t-1} + \frac{y_t - \tilde{x}_{t|t-1}}{m_t + \sigma_v^2} \mathbf{m}_t, \quad (\text{A34})$$

$$\mathbf{P}_t = \mathbf{M}_t - \frac{1}{m_t + \sigma_v^2} \mathbf{m}_t \mathbf{m}_t^T, \quad (\text{A35})$$

where vector \mathbf{m}_t is the first column of \mathbf{M}_t . Martin (1979), and Martin and Thomson (1982) proposed an approximate conditional mean robust filter based on Eq. (A34):

$$\hat{\mathbf{x}}_{t|t} = \tilde{\mathbf{x}}_{t|t-1} + \frac{\mathbf{m}_t}{\sqrt{m_t}} \psi\left(\frac{y_t - \tilde{x}_{t|t-1}}{\sqrt{m_t}}\right), \quad (\text{A36})$$

$$\psi(u) = \begin{cases} u & (|u| \leq a) \\ a(b-u)/(b-a) & (a < u \leq b) \\ -a(b+u)/(b-a) & (-b \leq u < -a) \\ 0 & (|u| > b) \end{cases} \quad (\text{A37})$$

In Eq. (A36), there is no information on the variance of V_t under the assumption that only a small fraction of time-series data is corrupted by outliers (Martin, 1979; Martin and Thomson, 1982). Eq. (A36) is equivalent to Eq. (A34) except for σ_v^2 if $|y_t - \tilde{x}_{t|t-1}| \leq a\sqrt{m_t}$. Using Eq. (A36), the first component of $\hat{\mathbf{x}}_{t|t}$, denoted by $\hat{x}_{t|t}$, follows the equation

$$\hat{x}_{t|t} = \begin{cases} y_t & (|y_t - \tilde{x}_{t|t-1}| \leq a\sqrt{m_t}) \\ \tilde{x}_{t|t-1} & (|y_t - \tilde{x}_{t|t-1}| > a\sqrt{m_t}) \end{cases} \quad (\text{A38})$$

That is, the robust filter replaces an observed value with its estimate based on previous values if the difference between them is large, whereas the observed value is not altered if the difference is small. Martin and Thomson (1982) replaced Eq. (A35) with

$$\mathbf{P}_t = \mathbf{M}_t - \chi \left(\frac{y_t - \tilde{x}_{t|t-1}}{\sqrt{m_t}} \right) \frac{\mathbf{m}_t \mathbf{m}_t^T}{m_t}, \quad (\text{A39})$$

$$\chi(u) = \frac{\psi(u)}{u} = \begin{cases} 1 & (|u| \leq a) \\ (b/u - 1)/(b/a - 1) & (a < u \leq b) \\ -(b/u + 1)/(b/a - 1) & (-b \leq u < -a) \\ 0 & (|u| > b) \end{cases} \quad (\text{A40})$$

Eq. (A39) is equivalent to Eq. (A35) except for σ_v^2 if $|y_t - \tilde{x}_{t|t-1}| \leq a\sqrt{m_t}$.

In this study, the first component of the state vector is used as the filtered value, as in Martin and Thomson (1982), that is,

$$\hat{x}_{t|t} = \tilde{x}_{t|t-1} + \sqrt{m_t} \psi \left(\frac{y_t - \tilde{x}_{t|t-1}}{\sqrt{m_t}} \right), \quad (\text{A41})$$

The minimum variance obtained by the S-estimator in estimating the AR coefficient is used as the variance σ_ε^2 in Eq. (A30). To prevent true signals from being unintentionally altered by the robust filter, large values are used for the parameters a and b in Eqs. (A37) and (A40). Specifically, a and b are fixed at 10 and 12, respectively. The median of the first p -th components of the original data is used for all elements of $\hat{\mathbf{x}}_{0|0}$, and the autocovariance matrix for the original time series estimated by the S-estimator (Maronna *et al.*, 2019) is used as \mathbf{P}_0 . As Maronna *et al.* (2019) suggested, when observed values are altered a sufficient number (k) of times consecutively, i.e., $\hat{x}_{t|t} \neq y_t$ for $t = t_0, \dots, t_0 + k$, the procedure returns to t_0 and restarts the recursions from $\hat{x}_{t_0|t_0} = y_{t_0}$. The value of k is fixed at 50 in this study.

(Received September 4, 2024)

(Accepted January 15, 2025)